Journal of Computational Physics 235 (2013) 846–864

Contents lists available at SciVerse ScienceDirect

Journal of Computational Physics

journal homepage: www.elsevier.com/locate/jcp

A pseudo-spectral method for the simulation of poro-elastic seismic wave propagation in 2D polar coordinates using domain decomposition

Rolf Sidler [a,*], José M. Carcione [b], Klaus Holliger [a]

[a] Center for Research of the Terrestrial Environment, University of Lausanne, CH-1015 Lausanne, Switzerland
[b] Istituto Nazionale di Oceanografia e di Geofisica Sperimentale (OGS), Borgo Grotta Gigante 42c, 34010 Sgonico, Trieste, Italy

ARTICLE INFO

Article history:
Received 7 February 2012
Received in revised form 27 September 2012
Accepted 28 September 2012
Available online 17 October 2012

Keywords:
Wave propagation
Poro-elasticity
Domain decomposition
Pseudo-spectral methods
Polar coordinates
Method of characteristics

ABSTRACT

We present a novel numerical approach for the comprehensive, flexible, and accurate simulation of poro-elastic wave propagation in 2D polar coordinates. An important application of this method and its extensions will be the modeling of complex seismic wave phenomena in fluid-filled boreholes, which represents a major, and as of yet largely unresolved, computational problem in exploration geophysics. In view of this, we consider a numerical mesh, which can be arbitrarily heterogeneous, consisting of two or more concentric rings representing the fluid in the center and the surrounding porous medium. The spatial discretization is based on a Chebyshev expansion in the radial direction and a Fourier expansion in the azimuthal direction and a Runge–Kutta integration scheme for the time evolution. A domain decomposition method is used to match the fluid–solid boundary conditions based on the method of characteristics. This multi-domain approach allows for significant reductions of the number of grid points in the azimuthal direction for the inner grid domain and thus for corresponding increases of the time step and enhancements of computational efficiency. The viability and accuracy of the proposed method has been rigorously tested and verified through comparisons with analytical solutions as well as with the results obtained with a corresponding, previously published, and independently benchmarked solution for 2D Cartesian coordinates. Finally, the proposed numerical solution also satisfies the reciprocity theorem, which indicates that the inherent singularity associated with the origin of the polar coordinate system is adequately handled.

1. Introduction

The comprehensive simulation of seismic wave propagation in realistic, highly heterogeneous borehole environments represents a pertinent and as of yet largely unresolved problem in exploration geophysics [1–3]. To address this issue, we have developed a method for the simulation of poro-elastic seismic wave propagation in 2D polar coordinates based on Biot's dynamic equations [4–7], which is an essential step towards constructing a full 3-D cylindrical algorithm for simulating borehole seismic experiments, such as sonic logging and vertical seismic profiling. In addition to the simulation of borehole seismic experiments *sensu strictu*, possible applications of this approach and its extensions can, for example, be found in the planning and/or evaluation of laboratory-scale experiments, the development of borehole seismic tools, or the optimized design of borehole casings. The use of a poro-elastic approach is essential given that a key objective of borehole seismic experiments is the estimation of the governing hydraulic characteristics of the surrounding geological formations [8–11]. The use of 2D polar coordinates for the development of our solution is motivated (i) by the inherent complexity of the derivation of

* Corresponding author.
E-mail address: rsidler@gmail.com (R. Sidler).

0021-9991/$ - see front matter © 2012 Elsevier Inc. All rights reserved.
http://dx.doi.org/10.1016/j.jcp.2012.09.044

the governing equations and the boundary conditions as well as their benchmarking and (ii) by the relative ease of the extension of a corresponding algorithm to 3D cylindrical coordinates [12,13].

Previous works have considered axisymmetric propagation in the vertical plane of the borehole [12,13], while the equivalent poro-elastic problem in Cartesian coordinates has been solved by Sidler [14]. The problem of 2D elastic wave propagation in polar coordinates based on the use of pseudo-spectral differential operators was first addressed by Kessler and Kosloff [15], who used Chebyshev and Fourier spatial differential operators in the radial and azimuthal directions, respectively. Here, we generalize this approach to the poro-elastic case, with an inner mesh representing the fluid filling of the hypothetical borehole and one or more outer meshes to represent the surrounding porous medium.

The meshes of these domains are combined by decomposing the wavefields into incoming and outgoing wave modes at the interface between the fluid and the porous solid and by modifying these modes on the basis of the fluid/poro-elastic boundary conditions. The boundary conditions at fluid-poro-elastic interfaces can be of the open-pore, closed-pore, or mixed-pore type, according to the theory developed by Deresiewicz and Skalak [16]. A Runge–Kutta integration scheme is used to compute the time evolution of the wavefield.

In the following, we first derive the equations of motion for a Biot-type porous solid in polar coordinates, describe the numerical solution of these equations via a pseudo-spectral approach and evaluate the characteristic vector for the decomposition of the wavefield in the azimuthal direction at the interfaces. We compare the proposed seismograms obtained with the numerical solution in 2D polar coordinates to corresponding analytical and numerical solutions in 2D Cartesian coordinates [17,18]. Finally, we show synthetic seismograms of a hypothetical 2D borehole experiment with a quadrupole-type source and varying boundary conditions at the borehole wall.

2. Equations of motion for a porous solid

Biot's dynamic poro-elastic equations in vector notation are [4,6]

$$\nabla \cdot \boldsymbol{\tau} = (\rho \ddot{\mathbf{u}} + \rho_f \ddot{\mathbf{u}}_f) - \mathbf{f}, \tag{1}$$

$$-\nabla p = \rho_f \ddot{\mathbf{u}} + \frac{\mathcal{T}\rho_f}{\phi}\ddot{\mathbf{u}}_f + \frac{\eta}{\kappa}\dot{\mathbf{u}}_f - \mathbf{g}, \tag{2}$$

where $\mathbf{u}$ and $\mathbf{u}_f$ are the displacement vectors of the solid and fluid relative to the solid phase, respectively, defined as $\mathbf{u}_f = \phi(\mathbf{U} - \mathbf{u})$ with $\mathbf{U}$ denoting the fluid displacement vector and ϕ the porosity. The external sources acting on the porous frame and pore fluid are denoted as $\mathbf{f}$ and $\mathbf{g}$, respectively. The tensor $\boldsymbol{\tau}$ and the scalar p denote the total stress and the fluid pressure, respectively. The bulk density is given as

$$\rho = (1 - \phi)\rho_s + \phi\rho_f \tag{3}$$

with ρ_s and ρ_f denoting the corresponding densities of the grains and the pore fluid, respectively. The quantity η is the fluid viscosity, κ is the frame permeability, and $\mathcal{T}$ is known as the structure or tortuosity factor. A dot above a variable denotes its differentiation with respect to time.

The stress–strain relations are [6]

$$\boldsymbol{\tau} = [(E_m - 2\mu + M\alpha^2)\nabla \cdot \mathbf{u} + \alpha M\nabla \cdot \mathbf{u}_f]\mathbf{I} + \mu[\nabla\mathbf{u} + \nabla\mathbf{u}^\top], \tag{4}$$

$$-p = \alpha M\nabla \cdot \mathbf{u} + M\nabla \cdot \mathbf{u}_f, \tag{5}$$

where $\mathbf{I}$ denotes the identity matrix and μ is the shear modulus of the bulk material, which is considered to be equal to the shear modulus of the dry matrix. E_m is the dry rock fast P-wave modulus defined as

$$E_m = K_m + \frac{4}{3}\mu, \tag{6}$$

with K_m denoting the bulk modulus of the dry material. The quantity M is defined as

$$M = \left(\frac{\alpha - \phi}{K_s} + \frac{\phi}{K_f}\right)^{-1}, \tag{7}$$

where K_s and K_f are the bulk moduli of the solid grains and the pore fluid, respectively. The coefficient α is known as the effective stress coefficient of the bulk material and is given by

$$\alpha = 1 - \frac{K_m}{K_s}. \tag{8}$$

Let us define the solid and relative fluid particle velocity vectors as $\mathbf{v} = \dot{\mathbf{u}}$ and $\mathbf{q} = \dot{\mathbf{u}}_f$, respectively. The poro-elastic equations (1) and (2) can then be expressed in 2D polar coordinates (Appendix A).

$$\tau_{rr,r} + \frac{1}{r}\tau_{r\theta,\theta} + \frac{\tau_{rr} - \tau_{\theta\theta}}{r} = \rho\dot{v}_r + \rho_f\dot{q}_r - f_r, \tag{9}$$

$$\tau_{r\theta,r} + \frac{1}{r}\tau_{\theta\theta,\theta} = \rho\dot{v}_\theta + \rho_f\dot{q}_\theta - f_\theta, \tag{10}$$

$$-p_{,r} = \rho_f\dot{v}_r + \frac{\mathcal{T}\rho_f}{\phi}\dot{q}_r + \frac{\eta}{\kappa}q_r - g_r, \tag{11}$$

$$-\frac{1}{r}p_{,\theta} = \rho_f\dot{v}_\theta + \frac{\mathcal{T}\rho_f}{\phi}\dot{q}_\theta + \frac{\eta}{\kappa}q_\theta - g_\theta, \tag{12}$$

where the subscripts r and θ denote the radial and azimuthal coordinates, and "$,r$" and "$,\theta$" the corresponding derivatives. f and g refer to the external sources [N/m^3]. We rewrite these equations in the particle-velocity/stress formulation as

$$\dot{v}_r = \gamma_{11}\left(\tau_{rr,r} + \frac{\tau_{r\theta,\theta}}{r} + \frac{\tau_{rr} - \tau_{\theta\theta}}{r}\right) + \gamma_{12}\left(p_{,r} + \frac{\eta}{\kappa}q_r\right) + s_r, \tag{13}$$

$$\dot{v}_\theta = \gamma_{11}\left(\frac{\tau_{\theta\theta,\theta}}{r} + \tau_{r\theta,r}\right) + \gamma_{12}\left(\frac{p_{,\theta}}{r} + \frac{\eta}{\kappa}q_\theta\right) + s_\theta, \tag{14}$$

$$\dot{q}_r = -\gamma_{12}\left(\tau_{rr,r} + \frac{\tau_{r\theta,\theta}}{r} + \frac{\tau_{rr} - \tau_{\theta\theta}}{r}\right) + \gamma_{22}\left(p_{,r} + \frac{\eta}{\kappa}q_r\right) + t_r, \tag{15}$$

$$\dot{q}_\theta = -\gamma_{12}\left(\frac{\tau_{\theta\theta,\theta}}{r} + \tau_{r\theta,r}\right) + \gamma_{22}\left(\frac{p_{,\theta}}{r} + \frac{\eta}{\kappa}q_\theta\right) + t_\theta, \tag{16}$$

where

$$\gamma_{11} = \frac{\mathcal{T}}{\rho\mathcal{T} - \phi\rho_f}, \quad \gamma_{12} = \frac{\phi}{\rho\mathcal{T} - \phi\rho_f}, \quad \gamma_{22} = \left(\frac{\rho}{\rho_f}\right)\frac{\phi}{\phi\rho_f - \rho\mathcal{T}}, \tag{17}$$

and

$$s_r = \gamma_{11}f_r - \gamma_{12}g_r, \tag{18}$$

$$s_\theta = \gamma_{11}f_\theta - \gamma_{12}g_\theta, \tag{19}$$

$$t_r = -\gamma_{22}g_r - \gamma_{12}f_r, \tag{20}$$

$$t_\theta = -\gamma_{22}g_\theta - \gamma_{12}f_\theta. \tag{21}$$

Similarly, the stress–strain relations (4) and (5) can be expressed as

$$\dot{\tau}_{rr} = (E_m - 2\mu + M\alpha^2)\nabla\cdot\mathbf{v} + \alpha M\nabla\cdot\mathbf{q} + 2\mu v_{r,r}, \tag{22}$$

$$\dot{\tau}_{\theta\theta} = (E_m - 2\mu + M\alpha^2)\nabla\cdot\mathbf{v} + \alpha M\nabla\cdot\mathbf{q} + \frac{2\mu}{r}(v_{\theta,\theta} + v_r), \tag{23}$$

$$\dot{\tau}_{r\theta} = \mu\left[\frac{1}{r}(v_{r,\theta} - v_\theta) + v_{\theta,r}\right], \tag{24}$$

$$\dot{p} = -M[\nabla\cdot\mathbf{q} + \alpha(\nabla\cdot\mathbf{v})], \tag{25}$$

where

$$\nabla\cdot\mathbf{v} = \frac{1}{r}(r\cdot v_r)_{,r} + \frac{1}{r}v_{\theta,\theta} \tag{26}$$

and

$$\nabla\cdot\mathbf{q} = \frac{1}{r}(r\cdot q_r)_{,r} + \frac{1}{r}q_{\theta,\theta}. \tag{27}$$

The equations of motion for the acoustic domain in the center with a fluid of density ρ_a and bulk modulus K_a are given by the stress–strain relation

$$\dot{p}_a = K_a\left[w_{r,r} + \frac{1}{r}(w_{\theta,\theta} + w_r)\right], \tag{28}$$

and Euler's equations

$$p_{a,r} = \rho_a\dot{w}_r, \quad \frac{1}{r}p_{a,\theta} = \rho_a\dot{w}_\theta, \tag{29}$$

where p_a and w denote the fluid pressure and particle velocities, respectively. Please note that in Eqs. (28) and (29) the subscript a and the symbol w for the particle velocity are used to distinguish the fluid of the acoustic domain from the fluid filling the pore space of the porous medium.

3. Numerical solution

Pseudo-spectral methods are efficient and highly accurate techniques for the modeling of complex wave propagation phenomena [6,14,15,19]. When there are physical boundary conditions to satisfy, the Fourier method is replaced by the Chebyshev method, which is not periodic and allows for the incorporation of boundary conditions by using characteristic variables. The presence of the slow diffusive compressional wave makes Biot's differential equations stiff. To overcome this problem, the corresponding equations are solved with the splitting scheme introduced by Carcione and Quiroga-Goode [17] where the stiff part of the equations is solved analytically for each time step. The numerical solution of the regular part of the differential equations is then obtained by using a 4th-order Runge–Kutta method for the time-stepping that uses four intermediate steps to calculate each time step. In complex environments this temporally sparse evaluation of the stiff part might lead to a reduction of numerical accuracy. A Chebyshev differential operator is used to compute the spatial derivatives along the radial direction, and a Fourier differential operator to compute the spatial derivatives along the azimuthal direction.

3.1. Characteristic variables

In order to model the fluid/porous-solid system, we use multiple grid domains, one for the fluid and another for the porous solid. The wavefield is decomposed into incoming and outgoing wave modes at the interface between the two media. The inward propagating waves depend on the solution exterior to the sub-domains and therefore are computed from the boundary conditions, while the behavior of the outward propagating waves is determined by the solution inside the sub-domains. The decomposition of the wavefield is based on the method of characteristics [14].

Let us compute the characteristics vector for the porous medium and fluid, respectively. The regular part of the poro-elastic equations (13)–(27), as characterized by $\eta = 0$, can be recast as

$$\mathbf{H}\dot{\mathbf{v}} = \mathbf{A}\mathbf{v}_{,r} + \mathbf{B}\mathbf{v}_{,\theta}, \tag{30}$$

where $\mathbf{H}, \mathbf{A}$, and $\mathbf{B}$ are matrices containing the material properties and

$$\mathbf{v} = (v_r, v_\theta, q_r, q_\theta, \tau_{rr}, \tau_{\theta\theta}, \tau_{r\theta}, p)^\top \tag{31}$$

is the field vector. The relevant matrix to implement the boundary conditions at the boundaries perpendicular to the r-direction is

$$\mathbf{A} = \begin{pmatrix} 0 & 0 & 0 & 0 & \gamma_{11} & 0 & 0 & \gamma_{12} \\ 0 & 0 & 0 & 0 & 0 & 0 & \gamma_{11} & 0 \\ 0 & 0 & 0 & 0 & -\gamma_{12} & 0 & 0 & \gamma_{22} \\ 0 & 0 & 0 & 0 & 0 & 0 & -\gamma_{12} & 0 \\ E_m + \alpha^2 M & 0 & \alpha M & 0 & 0 & 0 & 0 & 0 \\ E_m + \alpha^2 M - 2\mu & 0 & \alpha M & 0 & 0 & 0 & 0 & 0 \\ 0 & \mu & 0 & 0 & 0 & 0 & 0 & 0 \\ -\alpha M & 0 & -M & 0 & 0 & 0 & 0 & 0 \end{pmatrix}. \tag{32}$$

The characteristic vector is given by

$$\mathbf{c} = \mathbf{L}\mathbf{v}, \tag{33}$$

where $\mathbf{L}$ is the matrix whose rows are the left eigenvectors of matrix $\mathbf{A}$ (see Eq. (41) below). Vector $\mathbf{c}$ satisfies

$$\dot{\mathbf{c}} = \mathbf{\Lambda}\mathbf{c}_{,r}, \tag{34}$$

where the diagonal matrix $\mathbf{\Lambda}$ is given by

$$\mathbf{\Lambda} = \mathbf{L}\mathbf{A}\mathbf{L}^{-1}. \tag{35}$$

The eight eigenvalues, that is, the elements of $\mathbf{\Lambda}$, are given by

$$0; \quad 0; \quad \pm V_\pm; \quad \pm\sqrt{\gamma_{11}\mu}, \tag{36}$$

where

$$V_\pm = \sqrt{\frac{b \pm c}{2}}, \tag{37}$$

and

$$b = E_G\gamma_{11} - 2M\alpha\gamma_{12} - M\gamma_{22}, \tag{38}$$

with

$$E_G = E_m + \alpha^2 M \tag{39}$$

denoting the Gassmann P-wave modulus E_G. The scalar c, not to be confused with the characteristic vector $\mathbf{c}$, satisfies

$$b^2 - c^2 = 4M(M\alpha^2 - E_G)(\gamma_{12}^2 + \gamma_{11}\gamma_{22}). \tag{40}$$

The non-zero eigenvalues are the velocities of the ingoing and outgoing waves. The third set of eigenvalues corresponds to the fast and slow P-waves, as defined by the plus and minus signs inside the square root, respectively. Then follow the two eigenvalues corresponding to the ingoing and outgoing S-waves. The matrix $\mathbf{L}$ is given by

$$\mathbf{L} = \begin{pmatrix} 0 & 0 & 0 & 0 & l_{15} & 1 & 0 & l_{18} \\ 0 & l_{22} & 0 & 1 & 0 & 0 & 0 & 0 \\ l_{31} & 0 & l_{33} & 0 & l_{35} & 0 & 0 & l_{38} \\ -l_{31} & 0 & -l_{33} & 0 & l_{35} & 0 & 0 & l_{38} \\ l_{51} & 0 & l_{53} & 0 & -l_{35} & 0 & 0 & l_{58} \\ -l_{51} & 0 & -l_{53} & 0 & -l_{35} & 0 & 0 & l_{58} \\ 0 & l_{72} & 0 & 0 & 0 & 0 & \frac{1}{2} & 0 \\ 0 & -l_{72} & 0 & 0 & 0 & 0 & \frac{1}{2} & 0 \end{pmatrix}, \tag{41}$$

where

$$l_{15} = \frac{2eM}{V_+^2(c-b)}(M\alpha^2 - E_G + 2\mu), \tag{42}$$

$$l_{18} = \frac{4eM\alpha\mu}{V_+^2(c-b)}, \tag{43}$$

$$l_{22} = \frac{\gamma_{12}}{\gamma_{11}}, \tag{44}$$

$$l_{31} = -\frac{V_-}{4ce}[2M\alpha\gamma_{11}\gamma_{22} + \gamma_{12}(c + E_G\gamma_{11} - M\gamma_{22})], \tag{45}$$

$$l_{33} = -\frac{V_-}{4ce}\left[E_G\gamma_{11}^2 + (c - 2M\alpha\gamma_{12} + M\gamma_{22})\gamma_{11} + 2M\gamma_{12}^2\right], \tag{46}$$

$$l_{35} = \frac{M}{2c}(\alpha\gamma_{11} - \gamma_{12}), \tag{47}$$

$$l_{38} = \frac{c + E_G\gamma_{11} + M\gamma_{22}}{4c}, \tag{48}$$

$$l_{51} = -\frac{V_+}{4ce}[\gamma_{12}(c - E_G\gamma_{11} + M\gamma_{22}) - 2M\alpha\gamma_{11}\gamma_{22}], \tag{49}$$

$$l_{53} = -\frac{V_+}{4ce}\left[-E_G\gamma_{11}^2 + (c + 2M\alpha\gamma_{12} - M\gamma_{22})\gamma_{11} - 2M\gamma_{12}^2\right], \tag{50}$$

$$l_{58} = \frac{c - E_G\gamma_{11} - M\gamma_{22}}{4c}, \tag{51}$$

$$l_{72} = -\frac{1}{2}\sqrt{\frac{\mu}{\gamma_{11}}}, \tag{52}$$

with

$$e = \gamma_{12}^2 + \gamma_{11}\gamma_{22}. \tag{53}$$

Hence, the characteristic vector (33) is given by

$$\mathbf{c} = \begin{pmatrix} c_1 \\ c_2 \\ c_3 \\ c_4 \\ c_5 \\ c_6 \\ c_7 \\ c_8 \end{pmatrix} = \begin{pmatrix} l_{15}\tau_{rr} + \tau_{\theta\theta} + l_{18}p \\ l_{22}v_\theta + q_\theta \\ l_{31}v_r + l_{33}q_r + l_{35}\tau_{rr} + l_{38}p \\ -l_{31}v_r - l_{33}q_r + l_{35}\tau_{rr} + l_{38}p \\ l_{51}v_r + l_{53}q_r - l_{35}\tau_{rr} + l_{58}p \\ -l_{51}v_r - l_{53}q_r - l_{35}\tau_{rr} + l_{58}p \\ l_{72}v_\theta + \tau_{r\theta}/2 \\ -l_{72}v_\theta + \tau_{r\theta}/2 \end{pmatrix}. \tag{54}$$

It can be shown that the first two rows are the zero-eigenvalue characteristics, the third and fourth rows correspond to the slow P-waves, the fifth and sixth rows to the fast P-waves, and the seventh and eighth rows to the ingoing and outgoing S-waves, respectively [20,21].

Let us now consider the same approach for the acoustic equations of motion in the fluid domain (28) and (29). It is easy to show that the characteristics vector corresponding to the unknown vector $(w_r, w_\theta, p_a)^\top$ and the matrix

$$\mathbf{A} = \begin{pmatrix} 0 & 0 & \rho_a^{-1} \\ 0 & 0 & 0 \\ 0 & K_a & 0 \end{pmatrix} \tag{55}$$

is

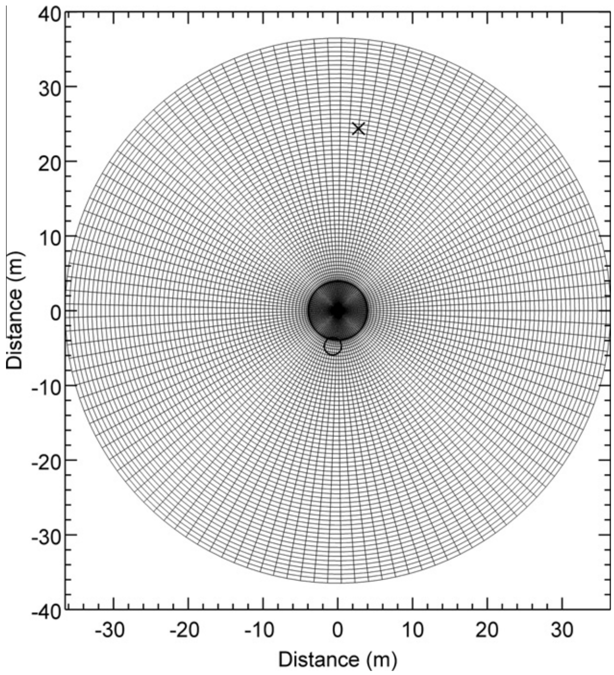

Fig. 1. Geometrical setup of the experiments to test the viability and accuracy of the numerical solution (Figs. 2–4). Cross and circle denote the locations of the source and receiver, respectively. The boundary between the two porous domains is located at a radial distance of 4 m.

Table 1
Poro-acoustic material properties of an unconsolidated sand [26].

Grain	Bulk modulus, K_s	32 GPa
	Density, ρ_s	2690 kg/m^3
Matrix	Bulk modulus, K_m	1.36 GPa
	Porosity, ϕ	0.38
	Permeability, κ	28.3 D $\cong 2.79 \cdot 10^{-11}$ m^2
	Tortuosity, $\mathcal{T}$	1.79
Fluid	Density, ρ_f	1000 kg/m^3
	Viscosity, η	0 Pa s
	Bulk modulus, K	2.25 GPa

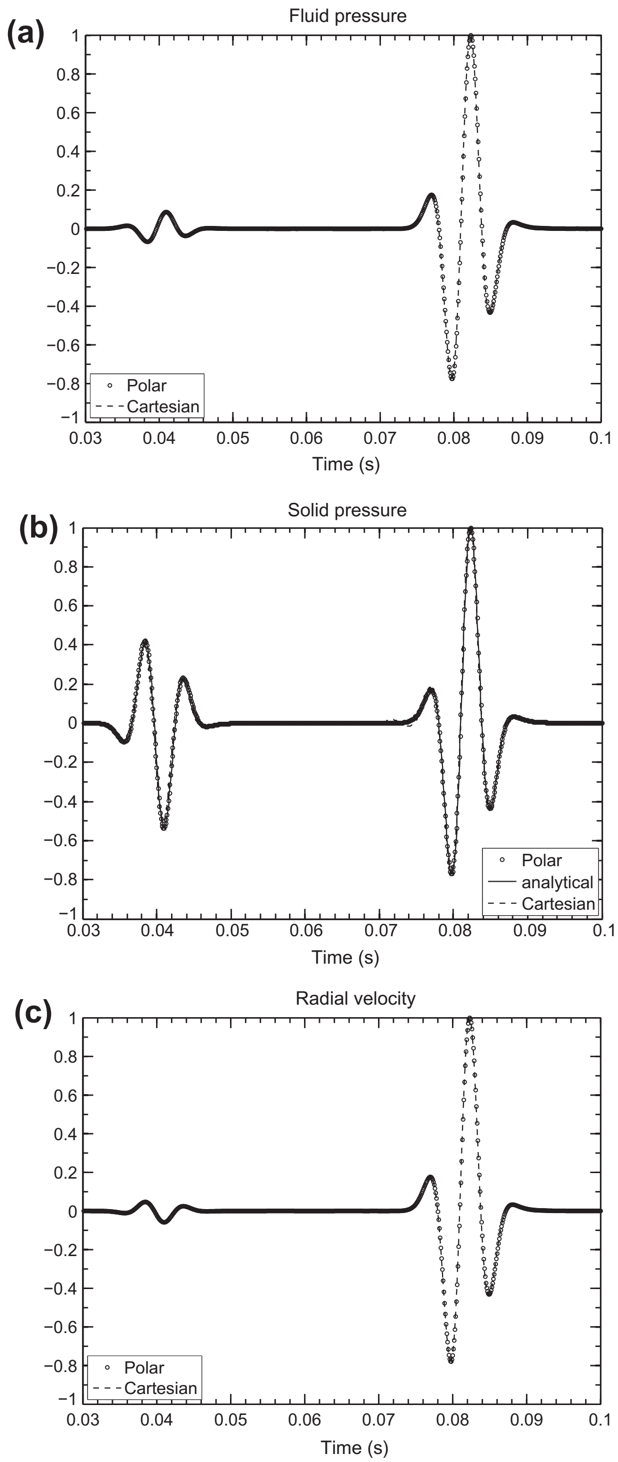

Fig. 2. Comparison between the analytical solution (solid line) and the numerical solutions in 2D polar (dots) and 2D Cartesian coordinates (dashed line) for (a) fluid pressure, (b) solid pressure, and (c) radial particle velocity. The material properties correspond to those of an unconsolidated sand saturated with a non-viscous pore fluid (Table 1). The analytical solution is only available for the solid pressure [18].

$$\mathbf{d} = \begin{pmatrix} d_1 \\ d_2 \\ d_3 \end{pmatrix} = \frac{1}{2}\begin{pmatrix} 2w_\theta \\ p_a - I_f w_r \\ p_a + I_f w_r \end{pmatrix}, \tag{56}$$

where d_1 is the characteristic in the azimuthal direction, while d_2 and d_3 are the inward and outward characteristics along the radial direction, respectively, and $I_f = \sqrt{\rho_a K_a}$ is the fluid impedance [14].

The equations defining the boundary conditions at different physical and non-physical boundaries are given in Appendix B and the wavefields at the grid points of such boundaries have to be modified according to these equations at each of the four intermediate time steps of the Runge–Kutta scheme. The types of boundaries considered are (Appendix B):

(i) free-surface of a porous solid,
(ii) interface between a fluid and a porous solid,
(iii) interfaces between two porous solids,
(iv) rigid boundary conditions for a fluid,
(v) non-reflecting, that is, absorbing, boundaries in a fluid and/or in a porous solid .

The latter type of boundary conditions is used to reduce non-physical reflections from the edges of the computational domain. Since these boundary conditions strictly remove only the wave components normal to the boundary, we use an additional damping strip at the outermost edge of the computational domain to effectively remove any undesired boundary reflections.

The use of multiple domains in polar coordinates is not only necessary to account for non-continuous field variables at physical interfaces, such as, for example, a fluid/porous-solid boundary or an abrupt change in porosity in a porous medium, but it is also advantageous in terms of computational cost. The angular grid spacing at the outer boundary of the computational domain is governed by the number of grid points needed to accurately simulate wave propagation through the considered model. Conversely, the angular grid spacing in the center of the domain becomes naturally much denser than actually necessary from a numerical point of view. The use of a domain decomposition method allows us to reduce the number of angular grid points in the inner domain, which in turn allows us to use larger time steps. As a consequence, the number of grid points of the inner and outer domains vary and their nodes are radially shifted with regard to each other. We use trigonometric interpolation to obtain the field variables at the locations of opposite grid nodes [22]. As the grid nodes are equally spaced in the angular direction, we can use a discrete Fourier transform to perform this interpolation.

4. Simulations

4.1. Verification of the numerical solution

To test the viability and accuracy of the numerical approach described above, we compare the results to the analytical solution for poro-acoustic media proposed by Carcione and Quiroga-Goode [17], Diaz and Ezziani [18], de la Puente et al. [23] and to numerical wavefields obtained with a previously published pseudo-spectral method in 2D Cartesian coordinates [14]. The model setup for this test consists of two concentric connected porous solids with identical material properties. The objective of this setup is to demonstrate that the wavefield is not distorted by the decomposition procedure at the interface. Note that due to the inherent singularity at $r = 0$, the center of the inner domain has a circular hole, which for the purpose of these tests must be chosen small enough so that the waves are not affected by its presence. Fig. 1 shows the setup of the mesh with a source acting on pore fluid pressure located at a radial distance of 24.51 m from the center and a receiver deployed on the opposite side of the inner porous domain at a distance of 4.80 m. The boundary between the porous domains is located at a radial distance of 4.00 m. The source mechanism corresponds to a fluid injection [24], that is, to a fluid-pressure-type excitation, whose time history is that of a Ricker wavelet with a central frequency of 125 Hz. The material properties of the porous medium are those of an unconsolidated sand saturated with a non-viscous, water-type liquid (Table 1).

Fig. 2 shows the pertinent components of the resulting analytical and numerical wavefields. We see that the seismograms obtained with the proposed numerical solution are indeed in excellent agreement with those obtained for corresponding analytical solutions as well as for the numerical solutions in 2D cartesian coordinates. The corresponding computations for a sandstone saturated with a viscous pore fluid (Table 2) are shown in Fig. 3. Again, we observe that the solution obtained

Table 2
Poro-elastic material properties of a sandstone [27].

Grain	bulk modulus, K_s	32 GPa
	Density, ρ_s	2480 kg/m^3
Matrix	Bulk modulus, K_m	6.1 GPa
	Porosity, ϕ	0.25
	Permeability, κ	1 D $\cong 9.8623 \cdot 10^{-13}$ m^2
	Tortuosity, $\mathcal{T}$	1.79
Fluid	Density, ρ_f	1000 kg/m^3
	Viscosity, η	0.001 Pa s
	Bulk modulus, K	2.25 GPa

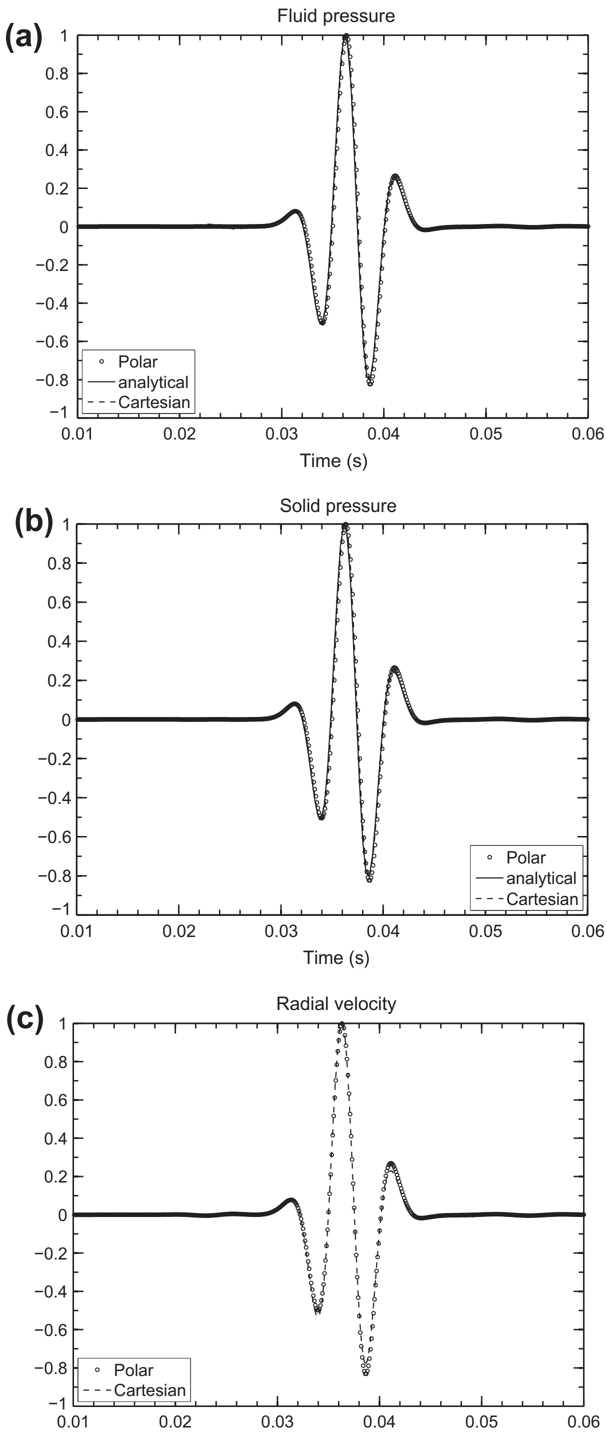

Fig. 3. Comparison between the analytical solution (solid line) and the numerical solutions in 2D polar (dots) and 2D Cartesian coordinates (dashed line) for (a) fluid pressure, (b) solid pressure, and (c) radial particle velocity. The material properties correspond to those of a sandstone saturated with a viscous pore fluid (Table 2). The analytical solution is only available for the fluid and solid pressures [17].

with the proposed numerical solution is in excellent agreement with the corresponding analytical and Cartesian numerical solution. We used the analytical solution of Diaz and Ezziani [18] for the comparison in Fig. 2 and the implementation of de la Puente et al. [23] for the analytical solution of Carcione and Quiroga-Goode [17] for the comparison in Fig. 3.

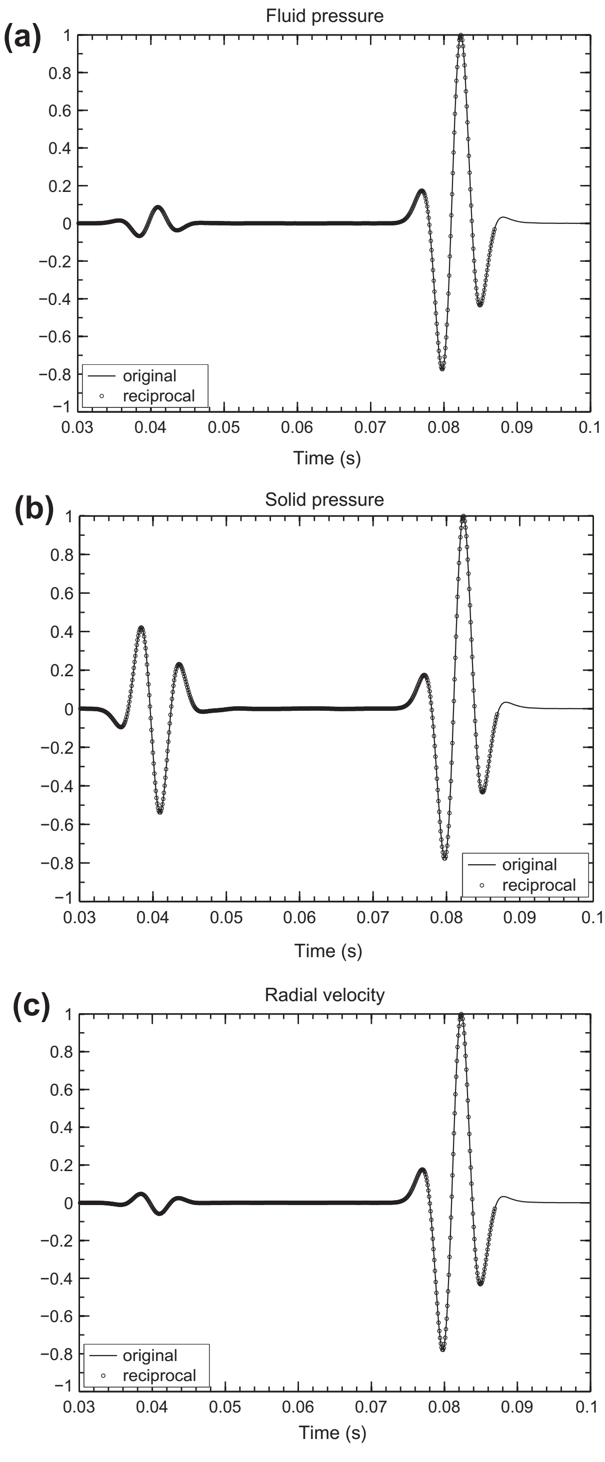

Fig. 4. Reciprocity experiment for the same model configuration used in the first example (Figs. 1 and 2). The solid line corresponds the solution for original configuration and is identical to that shown in Fig. 2; dots denote the corresponding reciprocal solution obtained by exchanging the source and receiver positions.

In Fig. 4 we show the results of a test with regard to the validity of the reciprocity principle. Due to the use of a fluid injection source, which has a monopole radiation pattern, the directivity of the source can be neglected and only the source and the receiver positions in the first experiment (Figs. 1 and 2) have to be exchanged. This test is important to assure that the inherent singularity at the origin of the polar coordinate system is adequately handled numerically

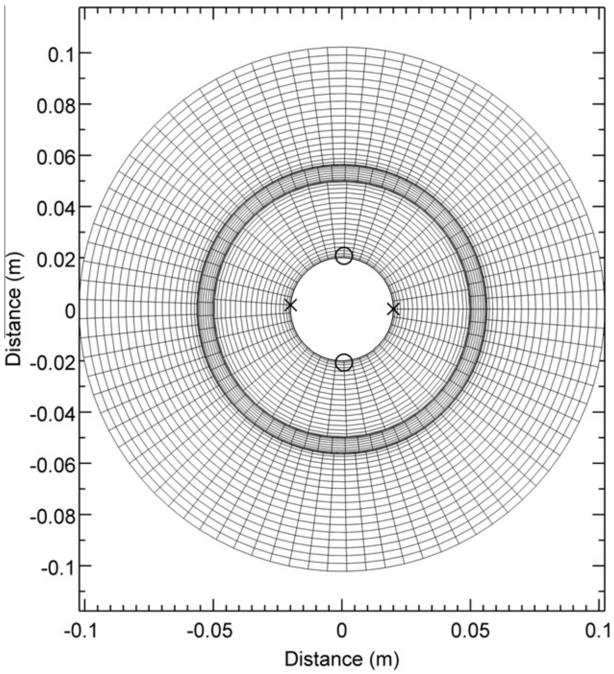

Fig. 5. Geometrical setup for the borehole experiments. The quadrupole-type fluid injection source (x–x) and the receivers (O) are located on the rigid inner boundary of the acoustic domain.

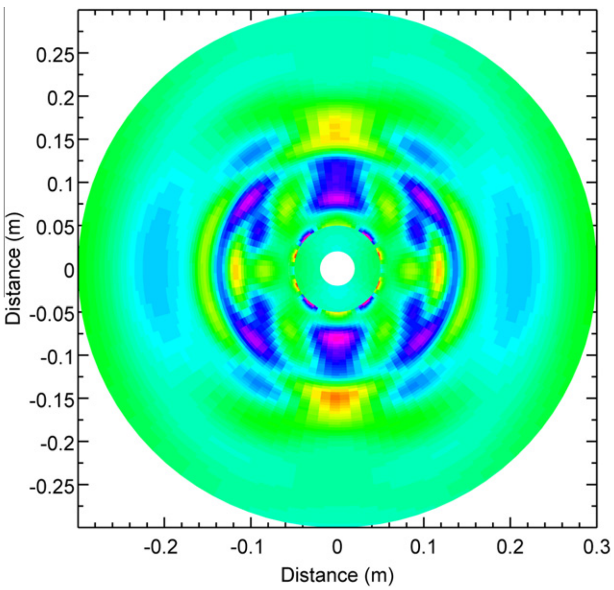

Fig. 6. Snapshot of the pressure field after a propagation time of 300 μs for the model containing no casing and open-pore boundary conditions (Figs. 5 and 7, Table 1).

[25]. The reason is that potential variations related to this feature would be different for the two solutions due to differing distances between the sources and the central singularity. The perfect conformity of the reciprocal solutions shows that the hole associated with the singularity can indeed be chosen small enough to avoid any distorting effects on the resulting seismograms.

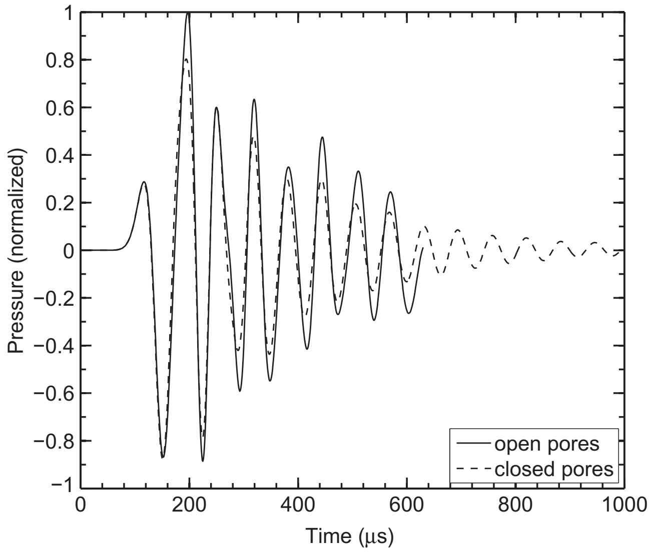

Fig. 7. Recordings of the fluid pressure in a borehole without casing (Fig. 5, Table 1). The solid line correspond to open-pore boundary conditions, while the dashed line represents closed-pore conditions. The recordings are normalized with respect to the maximum amplitude.

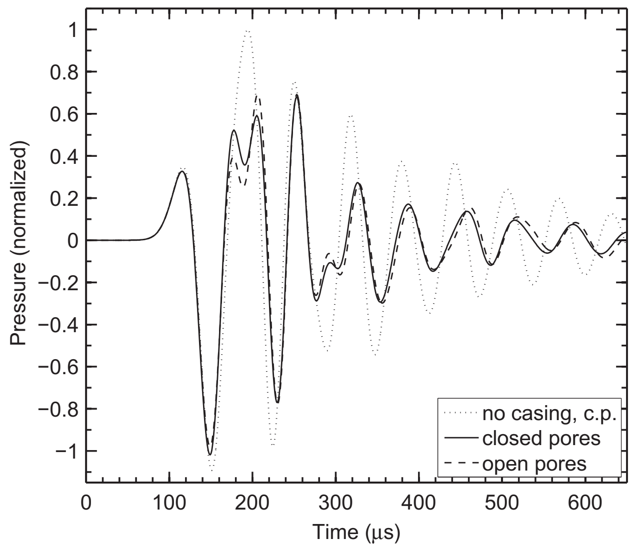

Fig. 8. Comparison of the fluid pressure recordings in a borehole in the presence and in the absence of a casing (Fig. 5, Tables 1 and 3). Both closed-pore as well as open-pore boundary conditions for the cased borehole are shown. The permeability of the casing in this experiment is 130 D. The data are normalized with respect to the maximum amplitude.

4.2. Solutions for a quadrupole-type source

In the following simulations, we consider an acoustic inner domain surrounded by one or several porous solids in analogy to a horizontal cross-section through a vertical fluid-filled borehole. The interface between the acoustic and the porous domain satisfies open-pore boundary conditions, where the surface flow impedance T is zero and closed-pore boundary conditions, where the surface flow impedance is infinitely large.

We consider a source that corresponds to a fluid volume injection on two opposite sides of the inner rigid boundary. Although the resulting radiation pattern strongly resembles a quadrupole source, this is neither a quadrupole source, as the two poles of opposite polarizations are missing and cannot be modeled using quadrupole symmetry, nor is it a dipole source as the two poles have the same polarity. Due to the 2D nature of the modeling domain, the sources are assumed to extend infinitely along the borehole axis. Two receivers are aligned perpendicularly to the axis of fluid pressure excitation. The overall model setup is shown in Fig. 5 and consists of three domains in order to adequately model a casing between the fluid and the surrounding porous solid.

Table 3
Poro-elastic material properties of a screened PVC casing [1,28].

Grain	Bulk modulus, K_s	4.049 GPa
	Shear modulus, μ_s	1.248 GPa
	Density, ρ_s	1400 kg/m^3
Matrix	Bulk modulus, K_m	3.482 GPa
	Shear modulus, μ_m	1.211 GPa
	Porosity, ϕ	0.04/0.10
	Permeability, κ	130 D/1900 D (1 D = 9.86233 $\cdot$ 10^{-13} m^2)
	Tortuosity, $\mathcal{T}$	1.5
Fluid	Density, ρ_f	1000 kg/m^3
	Viscosity, η	0.001 Pa s
	Bulk modulus, K	2.25 GPa

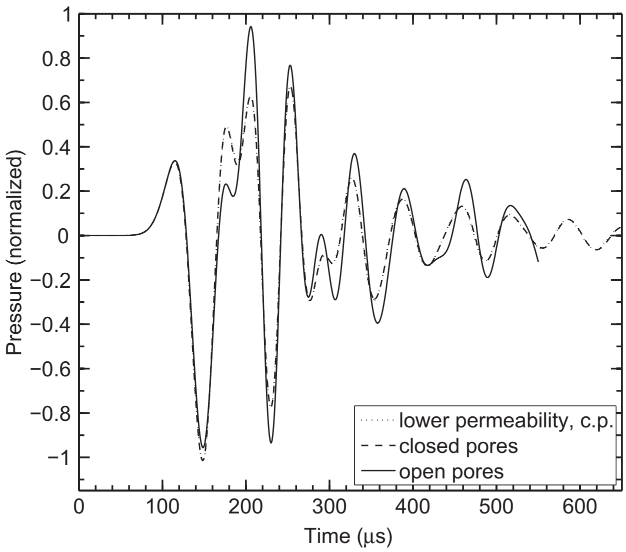

Fig. 9. Recordings of the fluid pressure in the presence of a casing characterized by a permeability of 1900 D (Fig. 5, Tables 1 and 3). The solution for both closed-pore and open-pore boundary conditions are shown. The closed-pore solution for a casing with permeability of 130 D (Fig. 8) is also shown and coincides with the closed pore solution of the casing with 1900 D. The data is normalized with respect to the maximum amplitude.

In the first example, the fluid filling the borehole and the pores of the surrounding medium is water, the porous medium is an unconsolidated sand (Table 1), and there is no casing between the fluid-filled borehole and the porous formation. The radius of the borehole is 50 mm and the acoustic domain consists of 21 grid nodes in the radial direction and 41 grid nodes in the azimuthal direction. In this case, the hole in the center of the domain represents a hypothetical borehole logging tool and has a radius of 20 mm. The outer boundary of the tool is assumed to be rigid [12]. The first porous domain consists of 11 grid points in the radial direction and 65 grid points in the azimuthal direction. The outer radius of the first of the two porous domain is 56.2 mm, which corresponds to the outer radius of the casing. The second, outer porous domain has the same material properties and is discretized using 85 grid points in the radial direction and 85 grid points in the azimuthal direction. The outer radius of this domain is 30 cm. The time history of the source is a Ricker wavelet with a central frequency of 10 kHz acting on the fluid pressure at the rigid inner boundary of the acoustic domain. Fig. 6 shows a snapshot of the pressure field illustrating the complex source radiation pattern resulting from the interaction of the quadrupole-type source, the rigid inner boundary, and the fluid-filled borehole, while Fig. 7 compares the numerical solutions for open- and closed-pore boundary conditions. The closed pore case could for example represent the case of thin impermeable mud cake separating the borehole fluid from the surrounding porous formation. Both solutions exhibit a special reverberatory character related to the waveguide effects of the borehole wall and show small but consistent differences in terms of their amplitudes.

In the second example, we set the properties of the inner porous domain to those of PVC to emulate a typical casing used to stabilize boreholes in the unconsolidated surficial sediments. The thickness of this PVC casing is 0.62 cm. The material properties of PVC are largely adopted from Bakulin [1]. There are, however, differing opinions with regard to the hydraulic properties of typical screened PVC casings. For example, Bakulin [1] uses a porosity of 4 % and a permeability of 130 D, whereas Barrash [28] calculates the porosity of screened PVC tubing to be of the order of 10 % or less and estimates the permeability based on the analog of a fractured karstic medium to be $\sim$1900 D (Table 3). Fig. 8 compares the recordings in the presence of a casing with screened PVC with a permeability of 130 D with the corresponding recordings in the absence of a casing, whereas Fig. 9 shows the results for the same experiment assuming a permeability of 1900 D for the screened casing.

The solutions for both open- and closed-pore boundary conditions are displayed. Note that the closed-pore responses do not depend on the permeability. We see that the presence of a casing has a significant influence on the waveforms and amplitudes of the recorded pressure fields, whereas the influence of the permeability of the casing as well as the open- or closed-pore boundary conditions seem to be of subordinate importance. Despite their conceptual simplicity, these examples clearly illustrate both the inherent complexity of seismic wave phenomena in borehole-type environments as well as the potential of the proposed numerical technique for adequately simulating them.

5. Conclusions

We have presented a pseudo-spectral numerical solution of the poro-elastic equations in 2D polar coordinates. Using a domain decomposition technique allows for splitting the numerical grid into several concentric sub-domains. The interfaces between the various sub-domains are matched based on the method of characteristics to satisfy the physical boundary conditions. In view of the eventual goal of modeling seismic wave propagation in fluid-filled boreholes, but without any loss of generality, the innermost sub-domain is based on the acoustic wave equation. The discretization of the wavefield in the radial direction employs a Chebyshev differential operator, whereas periodic boundary conditions based on a Fourier expansion is used along the azimuthal direction. The resulting numerical approach has been successfully tested with regard to pertinent analytical solutions as well as with regard to a corresponding numerical solution for 2D Cartesian coordinates. Using the reciprocity principle, we have also verified that the algorithm handles the singularity at the origin of the polar coordinate system in an adequate manner. Several examples involving a central fluid-filled region, the presence or absence of a casing as well as open- and closed-pore boundary conditions demonstrate the potential of the numerical approach for the realistic modeling of complex seismic wave phenomena in heterogeneous borehole-type environments. For this purpose, the solution will need to be extended to 3D cylindrical coordinates by adding the axial dimension to the governing equations, which is expected to be relatively straightforward.

Acknowledgment

We wish to thank the editor Alvin Bayliss as well as two anonymous reviewers for their constructive comments and suggestions that helped to improve this paper. This work has been supported by a grant from the Swiss National Science Foundation and was partly funded by the EU CO2CARE project.

Appendix A. Differential operators in polar coordinates

The gradient of a scalar quantity f in polar coordinates (r, θ) is given by

$$\nabla f = f_{,r}\ \hat{\mathbf{e}}_r + \frac{1}{r} f_{,\theta}\ \hat{\mathbf{e}}_\theta, \tag{A.1}$$

where $\hat{\mathbf{e}}_r$ and $\hat{\mathbf{e}}_\theta$ are unit vectors along the radial and azimuthal directions, respectively, and the subscript "$, r$" denotes differentiation of the corresponding parameter with respect to the coordinate r. The gradient and divergence of a vector $\mathbf{v}$ are given by

$$\nabla \mathbf{v} = \begin{pmatrix} v_{r,r} & \frac{1}{r}(v_{r,\theta} - v_\theta) \\ v_{\theta,r} & \frac{1}{r}(v_{\theta,\theta} + v_r) \end{pmatrix} \tag{A.2}$$

and

$$\nabla \cdot \mathbf{v} = \frac{1}{r} \frac{\partial}{\partial r}(r \cdot v_r) + \frac{1}{r} \frac{\partial v_\theta}{\partial \theta}. \tag{A.3}$$

Appendix B. Boundary conditions

B.1. Free-surface boundary conditions

The boundary conditions at the open-pore free surface of a porous medium are

$$\tau_{rr} = \tau_{r\theta} = 0, \quad p = 0. \tag{B.1}$$

Let the superscripts "(old)" and "(new)" denote values of variables before and after the application of the boundary conditions at the inner boundary of the mesh. Retaining the inward characteristics yields

$$
\begin{aligned}
c_1^{(\mathrm{old})} &= \tau_{\theta\theta}^{(\mathrm{new})},\\
c_2^{(\mathrm{old})} &= l_{22}\,v_\theta^{(\mathrm{new})} + q_\theta^{(\mathrm{new})},\\
c_3^{(\mathrm{old})} &= l_{31}\,v_r^{(\mathrm{new})} + l_{33}q_r^{(\mathrm{new})},\\
c_5^{(\mathrm{old})} &= l_{51}\,v_r^{(\mathrm{new})} + l_{53}q_r^{(\mathrm{new})},\\
c_7^{(\mathrm{old})} &= l_{72}\,v_\theta^{(\mathrm{new})},
\end{aligned}
\tag{B.2}
$$

where $c_J^{(\mathrm{old})},\ J = 1,\ldots,7$ are the old components of the characteristic vector $\mathbf{c}$. Solving the system (B.2) gives the free-surface boundary equations for the inner boundary

$$
\begin{aligned}
v_r^{(\mathrm{new})} &= (l_{33}c_5^{(\mathrm{old})} - l_{53}c_3^{(\mathrm{old})})/(l_{33}l_{51} - l_{31}l_{53}),\\
v_\theta^{(\mathrm{new})} &= c_7^{(\mathrm{old})}/l_{72},\\
q_r^{(\mathrm{new})} &= (l_{51}c_3^{(\mathrm{old})} - l_{31}c_5^{(\mathrm{old})})/(l_{33}l_{51} - l_{31}l_{53}),\\
q_\theta^{(\mathrm{new})} &= c_2^{(\mathrm{old})} - c_7^{(\mathrm{old})}l_{22}/l_{72},\\
\tau_{rr}^{(\mathrm{new})} &= 0,\\
\tau_{\theta\theta}^{(\mathrm{new})} &= c_1^{(\mathrm{old})},\\
\tau_{r\theta}^{(\mathrm{new})} &= 0,\\
p^{(\mathrm{new})} &= 0.
\end{aligned}
\tag{B.3}
$$

Correspondingly, the boundary equations for the outer boundary are

$$
\begin{aligned}
v_r^{(\mathrm{new})} &= (l_{53}c_4^{(\mathrm{old})} - l_{33}c_6^{(\mathrm{old})})/(l_{33}l_{51} - l_{31}l_{53}),\\
v_\theta^{(\mathrm{new})} &= -c_8^{(\mathrm{old})}/l_{72},\\
q_r^{(\mathrm{new})} &= (l_{31}c_6^{(\mathrm{old})} - l_{51}c_4^{(\mathrm{old})})/(l_{33}l_{51} - l_{31}l_{53}),\\
q_\theta^{(\mathrm{new})} &= c_2^{(\mathrm{old})} + c_8^{(\mathrm{old})}l_{22}/l_{72},\\
\tau_{rr}^{(\mathrm{new})} &= 0,\\
\tau_{\theta\theta}^{(\mathrm{new})} &= c_1^{(\mathrm{old})},\\
\tau_{r\theta}^{(\mathrm{new})} &= 0,\\
p^{(\mathrm{new})} &= 0.
\end{aligned}
\tag{B.4}
$$

B.2. Fluid/porous-solid boundary conditions

Let us denote by p_a and p the fluid pressure in the fluid and porous medium domains, respectively. The boundary conditions at an interface between a porous medium and a fluid are

$$
q_r + v_r = w_r, \quad p_a - p = Tq_r, \quad \tau_{rr} = p_a, \quad \tau_{r\theta} = 0,
\tag{B.5}
$$

where T is the dimensionless surface flow impedance. $T = 0$ corresponds to the open-pore case, whereas $T = \infty$ corresponds to the closed-pore case.

The updated fields for the porous medium are

$$
\begin{aligned}
Dv_r^{(\mathrm{new})} &= c_5^{(\mathrm{old})}[-l_{33} + I_f l_{35} + (I_f + T)l_{38}] + c_3^{(\mathrm{old})}[I_f l_{35} + l_{53} - (I_f + T)l_{58}] + 2d_3^{(\mathrm{old})}\{-l_{38}l_{53} + l_{33}(l_{58} - l_{35}) + l_{35}[T(l_{38} + l_{58}) - l_{53}]\},\\
v_\theta^{(\mathrm{new})} &= \frac{c_7^{(\mathrm{old})}}{l_{72}}\\
Dq_r^{(\mathrm{new})} &= c_5^{(\mathrm{old})}[l_{31} - I_f(l_{35} + l_{38})] + 2d_3^{(\mathrm{old})}[(l_{35} + l_{38})l_{51} + l_{31}(l_{35} - l_{58})] - c_3^{(\mathrm{old})}(I_f l_{35} + l_{51} - I_f l_{58}),\\
q_\theta^{(\mathrm{new})} &= c_2^{(\mathrm{old})} - \frac{c_7^{(\mathrm{old})}l_{22}}{l_{72}}\\
D\tau_{rr}^{(\mathrm{new})} &= -I_f c_5^{(\mathrm{old})}(l_{31} - l_{33} + Tl_{38}) + I_f c_3^{(\mathrm{old})}(l_{51} - l_{53} + Tl_{58}) + 2d_3^{(\mathrm{old})}[-l_{33}l_{51} + Tl_{38}l_{51} + l_{31}(l_{53} - Tl_{58})],\\
D\tau_{\theta\theta}^{(\mathrm{new})} &= Dc_1^{(\mathrm{old})} + c_5^{(\mathrm{old})}\{l_{18}[(I_f + T)l_{31} - I_f(l_{33} + Tl_{35})] + I_f l_{15}(l_{31} - l_{33} + Tl_{38})\}\\
&\quad + 2d_3^{(\mathrm{old})}\{l_{18}[(l_{33} + Tl_{35})l_{51} + l_{31}(Tl_{35} - l_{53})] + l_{15}[(l_{33} - Tl_{38})l_{51} - l_{31}l_{53} + Tl_{31}l_{58}]\}\\
&\quad - c_3^{(\mathrm{old})}\{l_{18}[I_f Tl_{35} + (I_f + T)l_{51} - I_f l_{53}] + I_f l_{15}(l_{51} - l_{53} + Tl_{58})\},\\
\tau_{r\theta}^{(\mathrm{new})} &= 0,\\
Dp^{(\mathrm{new})} &= c_5^{(\mathrm{old})}[I_f(l_{33} + Tl_{35}) - (I_f + T)l_{31}] + c_3^{(\mathrm{old})}[I_f Tl_{35} + (I_f + T)l_{51} - I_f l_{53}] - 2d_3^{(\mathrm{old})}[(l_{33} + Tl_{35})l_{51} + l_{31}(Tl_{35} - l_{53})],
\end{aligned}
\tag{B.6}
$$

where

$$D = T[I_f l_{35}(l_{38} + l_{58}) + l_{38}l_{51} - l_{31}l_{58}] + I_f(l_{35} + l_{38})(l_{51} - l_{53}) - l_{33}(I_f l_{35} - I_f l_{58} + l_{51}) + l_{31}(I_f l_{35} - I_f l_{58} + l_{53}). \tag{B.7}$$

The updated fields for the fluid are

$$\begin{aligned} w_r^{(\mathrm{new})} &= v_r^{(\mathrm{new})} + q_r^{(\mathrm{new})}, \\ w_\theta^{(\mathrm{new})} &= w_\theta^{(\mathrm{old})}, \\ p_a^{(\mathrm{new})} &= \tau_{rr}^{(\mathrm{new})}. \end{aligned} \tag{B.8}$$

B.3. Boundary conditions between two porous media

Let us denote by (1) and (2) the inner and outer media, respectively. The boundary conditions between these two porous media can be obtained by retaining the first two characteristics and the outward characteristics $[c_1(1), c_2(1), c_4(1), c_6(1), c_8(1)]$ of the inner medium and the two first characteristics and the inward characteristics of the outer medium $[c_1(2), c_2(2), c_3(2), c_5(2), c_7(2)]$ and applying the open-pore boundary conditions [16].

$$v_r(1) = v_r(2), v_\theta(1) = v_\theta(2), q_r(1) = q_r(2), \tau_{rr}(1) = \tau_{rr}(2), \tau_{r\theta}(1) = \tau_{r\theta}(2) \tag{B.9}$$

The boundary equations are

$$\begin{aligned} v_r^{(\mathrm{new})}(1) &= v_r^{(\mathrm{new})}(2) \\ &= (c_5^{(\mathrm{old})}(2)((l_{38}(1)l_{53}(1) - l_{33}(1)l_{58}(1))l_{35}(2) - l_{35}(1)((l_{38}(1) + l_{58}(1))l_{33}(2) + (l_{33}(1) + l_{53}(1))l_{38}(2))))/D \\ &\quad + (c_3^{(\mathrm{old})}(2)(l_{38}(1)l_{53}(1)l_{35}(2) - l_{33}(1)l_{58}(1)l_{35}(2) + l_{35}(1)l_{38}(1)l_{53}(2) + l_{35}(1)l_{58}(1)l_{53}(2) + l_{35}(1)(l_{33}(1) \\ &\quad + l_{53}(1))l_{58}(2)))/D + (c_6^{(\mathrm{old})}(1)(-l_{35}(1)l_{38}(2)l_{53}(2) + l_{38}(1)l_{35}(2)(l_{33}(2) + l_{53}(2)) + l_{35}(1)l_{33}(2)l_{58}(2) \\ &\quad + l_{33}(1)l_{35}(2)(l_{38}(2) + l_{58}(2))))/D - (c_4^{(\mathrm{old})}(1)(l_{35}(1)l_{38}(2)l_{53}(2) + l_{58}(1)l_{35}(2)(l_{33}(2) + l_{53}(2)) \\ &\quad - l_{35}(1)l_{33}(2)l_{58}(2) + l_{53}(1)l_{35}(2)(l_{38}(2) + l_{58}(2))))/D, \\[1ex] v_\theta^{(\mathrm{new})}(1) &= v_\theta^{(\mathrm{new})}(2) = c_7^{(\mathrm{old})}(2)/(l_{72}(1) + l_{72}(2)) - c_8^{(\mathrm{old})}(1)/(l_{72}(1) + l_{72}(2)), \\[1ex] q_r^{(\mathrm{new})}(1) &= q_r^{(\mathrm{new})}(2) \\ &= -((c_5^{(\mathrm{old})}(2)(l_{38}(1)l_{51}(1)l_{35}(2) - l_{31}(1)l_{58}(1)l_{35}(2) - l_{35}(1)((l_{38}(1) + l_{58}(1))l_{31}(2) + (l_{31}(1) + l_{51}(1))l_{38}(2))))/D) \\ &\quad - (c_3^{(\mathrm{old})}(2)(l_{38}(1)l_{51}(1)l_{35}(2) - l_{31}(1)l_{58}(1)l_{35}(2) + l_{35}(1)l_{38}(1)l_{51}(2) + l_{35}(1)l_{58}(1)l_{51}(2) + l_{35}(1)(l_{31}(1) \\ &\quad + l_{51}(1))l_{58}(2)))/D - (c_6^{(\mathrm{old})}(1)(-l_{35}(1)l_{38}(2)l_{51}(2) + l_{38}(1)l_{35}(2)(l_{31}(2) + l_{51}(2)) + l_{35}(1)l_{31}(2)l_{58}(2) \\ &\quad + l_{31}(1)l_{35}(2)(l_{38}(2) + l_{58}(2))))/D - (c_4^{(\mathrm{old})}(1)(-l_{35}(1)l_{38}(2)l_{51}(2) - l_{58}(1)l_{35}(2)(l_{31}(2) + l_{51}(2)) \\ &\quad + l_{35}(1)l_{31}(2)l_{58}(2) - l_{51}(1)l_{35}(2)(l_{38}(2) + l_{58}(2))))/D, \\[1ex] q_\theta^{(\mathrm{new})}(1) &= c_2^{(\mathrm{old})}(1) - (c_7^{(\mathrm{old})}(2)l_{22}(1))/(l_{72}(1) + l_{72}(2)) + (c_8^{(\mathrm{old})}(1)l_{22}(1))/(l_{72}(1) + {}_{72}(2)), \\[1ex] \tau_{rr}^{(\mathrm{new})}(1) &= \tau_{rr}^{(\mathrm{new})}(2) \\ &= (c_5^{(\mathrm{old})}(2)(-l_{38}(1)l_{53}(1)l_{31}(2) + l_{33}(1)l_{58}(1)l_{31}(2) + l_{38}(1)l_{51}(1)l_{33}(2) - l_{31}(1)l_{58}(1)l_{33}(2) \\ &\quad + l_{33}(1)l_{51}(1)l_{38}(2) - l_{31}(1)l_{53}(1)l_{38}(2)))/D + (c_3^{(\mathrm{old})}(2)(l_{38}(1)l_{53}(1)l_{51}(2) - l_{33}(1)l_{58}(1)l_{51}(2) \\ &\quad - l_{38}(1)l_{51}(1)l_{53}(2) + l_{31}(1)l_{58}(1)l_{53}(2) - l_{33}(1)l_{51}(1)l_{58}(2) + l_{31}(1)l_{53}(1)l_{58}(2)))/D - (c_6^{(\mathrm{old})}(1) \\ &\quad \times (-l_{38}(1)l_{33}(2)l_{51}(2) - l_{33}(1)l_{38}(2)l_{51}(2) + l_{38}(1)l_{31}(2)l_{53}(2) + l_{31}(1)l_{38}(2)l_{53}(2) + l_{33}(1)l_{31}(2)l_{58}(2) \\ &\quad - l_{31}(1)l_{33}(2)l_{58}(2)))/D - (c_4^{(\mathrm{old})}(1)(l_{58}(1)l_{33}(2)l_{51}(2) + l_{53}(1)l_{38}(2)l_{51}(2) - l_{58}(1)l_{31}(2)l_{53}(2) \\ &\quad - l_{51}(1)l_{38}(2)l_{53}(2) - l_{53}(1)l_{31}(2)l_{58}(2) + l_{51}(1)l_{33}(2)l_{58}(2)))/D, \end{aligned} \tag{B.10}$$

$$\tau_{\theta\theta}^{(\mathrm{new})}(1) = c_1^{(\mathrm{old})}(1) + \frac{1}{D}c_5^{(\mathrm{old})}(2)(l_{18}(1)(-l_{35}(1)l_{53}(1)l_{31}(2) + l_{35}(1)(l_{31}(1) + l_{51}(1))l_{33}(2) - l_{31}(1)l_{53}(1)l_{35}(2) + l_{33}(1) \times(-l_{35}(1)l_{31}(2) + l_{51}(1)l_{35}(2))) + l_{15}(1)(l_{38}(1)l_{53}(1)l_{31}(2) - l_{33}(1)l_{58}(1)l_{31}(2) - l_{38}(1)l_{51}(1)l_{33}(2) + l_{31}(1)l_{58}(1)l_{33}(2) - l_{33}(1)l_{51}(1)l_{38}(2) + l_{31}(1)l_{53}(1)l_{38}(2))) + (1/D)c_3^{(\mathrm{old})}(2)(l_{18}(1)(l_{33}(1)l_{51}(1)l_{35}(2) - l_{31}(1)l_{53}(1)l_{35}(2) + l_{33}(1)l_{35}(1)l_{51}(2) + l_{35}(1)l_{53}(1)l_{51}(2) - l_{35}(1)(l_{31}(1) + l_{51}(1))l_{53}(2)) + l_{15}(1) \times(-l_{38}(1)l_{53}(1)l_{51}(2) + l_{33}(1)l_{58}(1)l_{51}(2) + l_{38}(1)l_{51}(1)l_{53}(2) - l_{31}(1)l_{58}(1)l_{53}(2) + l_{33}(1)l_{51}(1)l_{58}(2) - l_{31}(1)l_{53}(1)l_{58}(2))) - (1/D)c_6^{(\mathrm{old})}(1)(l_{18}(1)(-l_{35}(1)l_{33}(2)l_{51}(2) - l_{33}(1)l_{35}(2)(l_{31}(2) + l_{51}(2)) + l_{35}(1)l_{31}(2)l_{53}(2) + l_{31}(1)l_{35}(2)(l_{33}(2) + l_{53}(2))) + l_{15}(1)(l_{38}(1)l_{33}(2)l_{51}(2) + l_{33}(1)l_{38}(2)l_{51}(2) - l_{38}(1)l_{31}(2)l_{53}(2) - l_{31}(1)l_{38}(2)l_{53}(2) - l_{33}(1)l_{31}(2)l_{58}(2) + l_{31}(1)l_{33}(2)l_{58}(2))) - (1/D)c_4^{(\mathrm{old})}(1)(l_{18}(1) \times(-l_{35}(1)l_{33}(2)l_{51}(2) + l_{53}(1)l_{35}(2)(l_{31}(2) + l_{51}(2)) + l_{35}(1)l_{31}(2)l_{53}(2) - l_{51}(1)l_{35}(2)(l_{33}(2) + l_{53}(2))) + l_{15}(1) \times(-l_{58}(1)l_{33}(2)l_{51}(2) - l_{53}(1)l_{38}(2)l_{51}(2) + l_{58}(1)l_{31}(2)l_{53}(2) + l_{51}(1)l_{38}(2)l_{53}(2) + l_{53}(1)l_{31}(2)l_{58}(2) - l_{51}(1)l_{33}(2)l_{58}(2))),$$

$$\tau_{r\theta}^{(\mathrm{new})}(1) = \tau_{r\theta}^{(\mathrm{new})}(2) = (2c_7^{(\mathrm{old})}(2)l_{72}(1))/(l_{72}(1) + l_{72}(2)) + (2c_8^{(\mathrm{old})}(1)l_{72}(2))/(l_{72}(1) + l_{72}(2)),$$

$$p^{(\mathrm{new})}(1) = p^{(\mathrm{new})}(2) = (c_5^{(\mathrm{old})}(2)(l_{35}(1)l_{53}(1)l_{31}(2) - l_{35}(1)(l_{31}(1) + l_{51}(1))l_{33}(2) + l_{31}(1)l_{53}(1)l_{35}(2) + l_{33}(1)(l_{35}(1)l_{31}(2) - l_{51}(1)l_{35}(2))))/D - (c_3^{(\mathrm{old})}(2)(l_{33}(1)l_{51}(1)l_{35}(2) - l_{31}(1)l_{53}(1)l_{35}(2) + l_{33}(1)l_{35}(1)l_{51}(2) + l_{35}(1)l_{53}(1)l_{51}(2) - l_{35}(1)(l_{31}(1) + l_{51}(1))l_{53}(2)))/D - (c_6^{(\mathrm{old})}(1)(l_{35}(1)l_{33}(2)l_{51}(2) + l_{33}(1)l_{35}(2)(l_{31}(2) + l_{51}(2)) - l_{35}(1)l_{31}(2)l_{53}(2) - l_{31}(1)l_{35}(2)(l_{33}(2) + l_{53}(2))))/D + (c_4^{(\mathrm{old})}(1)(-l_{35}(1)l_{33}(2)l_{51}(2) + l_{53}(1)l_{35}(2)(l_{31}(2) + l_{51}(2)) + l_{35}(1)l_{31}(2)l_{53}(2) - l_{51}(1)l_{35}(2)(l_{33}(2) + l_{53}(2))))/D,$$

$$q_{\theta}^{(\mathrm{new})}(2) = c_2^{(\mathrm{old})}(2) - (c_7^{(\mathrm{old})}(2)l_{22}(2))/(l_{72}(1) + l_{72}(2)) + (c_8^{(\mathrm{old})}(1)l_{22}(2))/(l_{72}(1) + l_{72}(2)),$$

$$\tau_{\theta\theta}^{(\mathrm{new})}(2) = c_1^{(\mathrm{old})}(2) + (1/D)c_5^{(\mathrm{old})}(2)(-l_{35}(1)l_{53}(1)l_{18}(2)l_{31}(2) + l_{31}(1)l_{58}(1)l_{15}(2)l_{33}(2) + l_{31}(1)l_{35}(1)l_{18}(2)l_{33}(2) + l_{35}(1)l_{51}(1)l_{18}(2)l_{33}(2) + l_{38}(1)l_{15}(2)(l_{53}(1)l_{31}(2) - l_{51}(1)l_{33}(2)) - l_{31}(1)l_{53}(1)l_{18}(2)l_{35}(2) + l_{31}(1)l_{53}(1)l_{15}(2)l_{38}(2) - l_{33}(1)(l_{58}(1)l_{15}(2)l_{31}(2) + l_{35}(1)l_{18}(2)l_{31}(2) - l_{51}(1)l_{18}(2)l_{35}(2) + l_{51}(1)l_{15}(2)l_{38}(2))) - (1/D)c_3^{(\mathrm{old})}(2)((l_{38}(1)l_{15}(2) - l_{35}(1)l_{18}(2))(l_{53}(1)l_{51}(2) - l_{51}(1)l_{53}(2)) - l_{33}(1) \times(l_{51}(1)l_{18}(2)l_{35}(2) + l_{58}(1)l_{15}(2)l_{51}(2) + l_{35}(1)l_{18}(2)l_{51}(2) + l_{51}(1)l_{15}(2)l_{58}(2)) + l_{31}(1)(l_{53}(1)l_{18}(2)l_{35}(2) + l_{58}(1)l_{15}(2)l_{53}(2) + l_{35}(1)l_{18}(2)l_{53}(2) + l_{53}(1)l_{15}(2)l_{58}(2))) - (1/D)c_6^{(\mathrm{old})}(1)((l_{38}(1)l_{15}(2) - l_{35}(1)l_{18}(2)) \times(l_{33}(2)l_{51}(2) - l_{31}(2)l_{53}(2)) - l_{33}(1)(-l_{15}(2)l_{38}(2)l_{51}(2) + l_{18}(2)l_{35}(2)(l_{31}(2) + l_{51}(2)) + l_{15}(2)l_{31}(2)l_{58}(2)) + l_{31}(1)(-l_{15}(2)l_{38}(2)l_{53}(2) + l_{18}(2)l_{35}(2)(l_{33}(2) + l_{53}(2)) + l_{15}(2)l_{33}(2)l_{58}(2))) - (1/D)c_4^{(\mathrm{old})}(1)(-(l_{58}(1)l_{15}(2) + l_{35}(1)l_{18}(2))(l_{33}(2)l_{51}(2) - l_{31}(2)l_{53}(2)) + l_{53}(1)(-l_{15}(2)l_{38}(2)l_{51}(2) + l_{18}(2)l_{35}(2)(l_{31}(2) + l_{51}(2)) + l_{15}(2)l_{31}(2)l_{58}(2)) - l_{51}(1)(-l_{15}(2)l_{38}(2)l_{53}(2) + l_{18}(2)l_{35}(2)(l_{33}(2) + l_{53}(2)) + l_{15}(2)l_{33}(2)l_{58}(2))),$$

with

$$D = (l_{31}(1)l_{58}(1)l_{33}(2)l_{35}(2) + l_{31}(1)l_{53}(1)l_{35}(2)l_{38}(2) - l_{35}(1)l_{58}(1)l_{33}(2)l_{51}(2) - l_{35}(1)l_{53}(1)l_{38}(2)l_{51}(2) + l_{35}(1)l_{58}(1)l_{31}(2)l_{53}(2) + l_{31}(1)l_{58}(1)l_{35}(2)l_{53}(2) + l_{31}(1)l_{35}(1)l_{38}(2)l_{53}(2) + l_{35}(1)l_{51}(1)l_{38}(2)l_{53}(2) + l_{38}(1) \times(-l_{35}(1)l_{33}(2)l_{51}(2) + l_{53}(1)l_{35}(2)(l_{31}(2) + l_{51}(2)) + l_{35}(1)l_{31}(2)l_{53}(2) - l_{51}(1)l_{35}(2)(l_{33}(2) + l_{53}(2))) + (l_{35}(1)l_{53}(1)l_{31}(2) - l_{35}(1)(l_{31}(1) + l_{51}(1))l_{33}(2) + l_{31}(1)l_{53}(1)l_{35}(2))l_{58}(2) - l_{33}(1)(l_{58}(1)l_{35}(2)(l_{31}(2) + l_{51}(2)) + l_{51}(1)l_{35}(2)(l_{38}(2) + l_{58}(2)) + l_{35}(1)(l_{38}(2)l_{51}(2) - l_{31}(2)l_{58}(2)))).$$

B.4. Rigid boundary conditions for a fluid

Rigid boundary conditions at the center of the fluid-filled domain are obtained by retaining the inward characteristics and $w_r = 0, w_\theta^{new} = w_\theta^{old}$ and are implemented as

$$
\begin{aligned}
w_\theta^{(\text{new})} &= w_\theta^{(\text{old})},\\
w_r^{(\text{new})} &= 0,\\
p_a^{(\text{new})} &= 2d_2^{(\text{old})}.
\end{aligned}
\tag{B.11}
$$

At the outer fluid boundary it would be

$$
\begin{aligned}
w_\theta^{(\text{new})} &= w_\theta^{(\text{old})},\\
w_r^{(\text{new})} &= 0,\\
p_a^{(\text{new})} &= 2d_3^{(\text{old})}.
\end{aligned}
\tag{B.12}
$$

B.5. Non-reflecting boundary conditions

The non-reflecting boundary conditions for the outer boundary of a porous medium can be obtained by retaining the first two characteristics and the outward characteristics and set the inward characteristics c_3, c_5, and c_7 to zero. This leads to the following boundary conditions for the outer boundary

$$
\begin{aligned}
2v_r^{(\text{new})} &= v_r^{(\text{old})} + \{(l_{38}l_{53} - l_{33}l_{58})p^{(\text{old})} + [l_{35}(l_{33} + l_{53})]\tau_{rr}^{(\text{old})}\}/(l_{33}l_{51} - l_{31}l_{53}),\\
2v_\theta^{(\text{new})} &= v_\theta^{(\text{old})} - \tau_{r\theta}^{(\text{old})}/(2l_{72}),\\
2q_r^{(\text{new})} &= q_r^{(\text{old})} + \{(l_{38}l_{51} - l_{31}l_{58})p^{(\text{old})} + [l_{35}(l_{31} + l_{51})]\tau_{rr}^{(\text{old})}\}/(-l_{33}l_{51} + l_{31}l_{53}),\\
q_\theta^{(\text{new})} &= q_\theta^{(\text{old})} + (l_{22}/2)v_\theta^{(\text{old})} + (l_{22}/4l_{72})\tau_{r\theta}^{(\text{old})},\\
2\tau_{rr}^{(\text{new})} &= \tau_{rr}^{(\text{old})} + [(l_{38}l_{53} - l_{33}l_{58})q_r^{(\text{old})} + (l_{38}l_{51} - l_{31}l_{58})v_r^{(\text{old})}]/(l_{35}(l_{38} + l_{58})),\\
2\tau_{\theta\theta}^{(\text{new})} &= l_{18}p^{(\text{old})} + l_{15}\tau_{rr}^{(\text{old})} + 2\tau_{\theta\theta}^{(\text{old})} + \{[l_{18}l_{35}(l_{33} + l_{53}) + l_{15}(-l_{38}l_{53} + l_{33}l_{58})]q_r^{(\text{old})}\\
&\quad + [l_{18}l_{35}(l_{31} + l_{51}) + l_{15}(-l_{38}l_{51} + l_{31}l_{58})]v_r^{(\text{old})}\}/(l_{35}(l_{38} + l_{58}))\\
2\tau_{r\theta}^{(\text{new})} &= -2l_{72}v_\theta^{(\text{old})} + \tau_{r\theta}^{(\text{old})},\\
2p^{(\text{new})} &= p^{(\text{old})} - [(l_{33} + l_{53})q_r^{(\text{old})} + (l_{31} + l_{51})v_r^{(\text{old})}]/(l_{38} + l_{58}).
\end{aligned}
\tag{B.13}
$$

The inner boundary conditions are

$$
\begin{aligned}
2v_r^{(\text{new})} &= v_r^{(\text{old})} + [p^{(\text{old})}(l_{38}l_{53} - l_{33}l_{58}) + \tau_{rr}^{(\text{old})}l_{35}(l_{33} + l_{53})]/(l_{31}l_{53} - l_{33}l_{51}),\\
2v_\theta^{(\text{new})} &= v_\theta^{(\text{old})} + \tau_{r\theta}^{(\text{old})}/(2l_{72}),\\
2q_r^{(\text{new})} &= q_r^{(\text{old})} + [p^{(\text{old})}(l_{38}l_{51} - l_{31}l_{58}) + \tau_{rr}^{(\text{old})}l_{35}(l_{31} + l_{51})]/(l_{33}l_{51} - l_{31}l_{53}),\\
q_\theta^{(\text{new})} &= q_\theta^{(\text{old})} + v_\theta^{(\text{old})}(l_{22}/2) - \tau_{r\theta}^{(\text{old})}l_{22}/(4l_{72}),\\
2\tau_{rr}^{(\text{new})} &= \tau_{rr}^{(\text{old})} + [q_r^{(\text{old})}(l_{33}l_{58} - l_{38}l_{53}) + v_r^{(\text{old})}(l_{31}l_{58} - l_{38}l_{51})]/[l_{35}(l_{38} + l_{58})],\\
2\tau_{\theta\theta}^{(\text{new})} &= p^{(\text{old})}l_{18} + \tau_{rr}^{(\text{old})}l_{15} + 2\tau_{\theta\theta}^{(\text{old})} + \{q_r^{(\text{old})}[l_{15}(l_{38}l_{53} - l_{33}l_{58}) - l_{18}l_{35}(l_{33} + l_{53})]\\
&\quad + v_r^{(\text{old})}[l_{15}(l_{38}l_{51} - l_{31}l_{58}) - l_{18}l_{35}(l_{31} + l_{51})]\}/(2l_{35}(l_{38} + l_{58})),\\
2\tau_{r\theta}^{(\text{new})} &= 2l_{72}v_\theta^{(\text{old})} + \tau_{r\theta}^{(\text{old})},\\
2p^{(\text{new})} &= p^{(\text{old})} + [q_r^{(\text{old})}(l_{33} + l_{53}) + v_r^{(\text{old})}(l_{31} + l_{51})]/(l_{38} + l_{58}).
\end{aligned}
\tag{B.14}
$$

On the other hand, the non-reflecting boundary conditions of the outer boundary of the fluid are

$$
\begin{aligned}
w_\theta^{(\text{new})} &= w_\theta^{(\text{old})},\\
w_r^{(\text{new})} &= d_3^{(\text{old})}/I_f,\\
p_a^{(\text{new})} &= d_3^{(\text{old})},
\end{aligned}
\tag{B.15}
$$

while those of the inner boundary are

$$
\begin{aligned}
w_\theta^{(\text{new})} &= w_\theta^{(\text{old})},\\
w_r^{(\text{new})} &= -d_2^{(\text{old})}/I_f,\\
p_a^{(\text{new})} &= d_2^{(\text{old})}.
\end{aligned}
\tag{B.16}
$$

References

[1] A. Bakulin, A. Sidorov, B. Kashtan, M. Jaaskelainen, Real-time completion monitoring with acoustic waves, Geophysics 73 (2008) E15–E33.
[2] M. Käser, C. Pelties, C.E. Castro, Wavefield modeling in exploration seismology using the discontinuous Galerkin finite-element method on HPC infrastructure, The Leading Edge 29 (2010) 76–85.
[3] F. Karpfinger, B. Gurevich, H.-P. Valero, A. Bakulin, B. Sinha, Tube wave signatures in cylindrically layered poroelastic media computed with spectral method, Geophysical Journal International 183 (2010) 1005–1013.
[4] M.A. Biot, Mechanics of deformation and acoustic propagation in porous media, Journal of Applied Physics 33 (1962) 1482–1498.
[5] M.A. Biot, Generalized theory of acoustic propagation in porous dissipative media, Journal of the Acoustical Society of America 34 (1962) 1254–1264.
[6] J.M. Carcione, Wave Fields in Real Media: Wave Propagation in Anisotropic, Anelastic, Porous and Electromagnetic Media, second ed., Elsevier, Amsterdam, 2007.
[7] C. Morency, J. Tromp, Spectral-element simulation of wave propagation in porous media, Geophysical Journal International 175 (2008) 301–345.
[8] A.N. Norris, Stoneley-wave attenuation and dispersion in permeable formations, Geophysics 54 (1989) 330–341.
[9] T. Klimentos, C. McCann, Relationships among compressional wave attenuation, porosity, clay content, and permeability in sandstones, Geophysics 55 (1990) 998–1014.
[10] X.M. Tang, A. Cheng, Quantitative Borehole Acoustic Methods, Handbook of Geophysical Exploration, Elsevier, 2004.
[11] L. Lin, M.L. Peterson, A.R. Greenberg, B.A. McCool, In situ measurement of permeability, Journal of the Acoustical Society of America 125 (2009) EL123.
[12] J.M. Carcione, F. Poletto, Synthetic logs of multipole sources in boreholes based on the Kelvin–Voigt stress–strain relation, Geophysical Journal International 174 (2008) 808–814.
[13] J.M. Carcione, F. Poletto, B. Farina, Simulation of axis-symmetric seismic waves in fluid-filled boreholes in the presence of a drill string, Computational Geosciences 12 (2008) 593–604.
[14] R. Sidler, J.M. Carcione, K. Holliger, Simulation of surface waves in porous media, Geophysical Journal International 183 (2010) 820–832.
[15] D. Kessler, D. Kosloff, Elastic wave propagation using cylindrical coordinates, Geophysics 56 (1991) 2080–2089.
[16] H. Deresiewicz, R. Skalak, On uniqueness in dynamic poroelasticity, Bulletin of the Seismological Society of America 53 (1963) 783–788.
[17] J.M. Carcione, G. Quiroga-Goode, Some aspects of the physics and numerical modeling of Biot compressional waves, Journal of Computational Acoustics 3 (1996) 261–280.
[18] J. Diaz, A. Ezziani, Analytical solution for waves propagation in heterogeneous acoustic/porous media. Part I: The 2D case, Communications in Computational Physics 7 (2010) 171–194.
[19] X. Liu, S. Greenhalgh, Y. Wang, 2.5-D poroelastic wave modelling in double porosity media, Geophysical Journal International 186 (2011) 1285–1294.
[20] D. Gottlieb, M. Gunzburger, E. Turkel, On numerical boundary treatment of hyperbolic systems for finite difference and finite element methods, SIAM Journal on Numerical Analysis 19 (1982).
[21] J.M. Carcione, Domain decomposition for wave propagation problems, Journal of Scientific Computing 6 (1991) 453–472.
[22] K.E. Atkinson, An Introduction to Numerical Analysis, second ed., Wiley and Sons, New York, 1989.
[23] J. de la Puente, M. Dumbser, M. Käser, H. Igel, Discontinuous Galerkin methods for wave propagation in poroelastic media, Geophysics 73 (2008) T77–T97.
[24] F. Karpfinger, Modelling borehole wave signatures in elastic and poroelastic media with spectral method, Ph.D. thesis, Curtin University of Technology, 2009.
[25] E. Tessmer, D. Kessler, D. Kosloff, A. Behle, Multi-domain Chebyshev–Fourier method for the solution of the equations of motion of dynamic elasticity, Journal of Computational Physics 100 (1992) 355–363.
[26] D.R. Jackson, M.D. Richardson, High-Frequency Seafloor Acoustics, Springer, New York, 2007.
[27] J.M. Carcione, H.B. Helle, N.H. Pham, White's model for wave propagation in partially saturated rocks: Comparison with poroelastic numerical experiments, Geophysics 68 (2003) 1389–1398.
[28] W. Barrash, T. Clemo, J.J. Fox, T.C. Johnson, Field, laboratory, and modeling investigation of the skin effect at wells with slotted casing, Boise Hydrogeophysical Research Site, Journal of Hydrology 326 (2006) 181–198.